



Exploring anomalous light dynamics around higher-order conjugate exceptional points with local nonlinearity

Sibnath Dey  and Somnath Ghosh **Unconventional Photonics Laboratory, Department of Physics, Indian Institute of Technology Jodhpur, Rajasthan-342037, India*

(Received 30 January 2023; revised 26 May 2023; accepted 25 July 2023; published 10 August 2023)

Dynamical encirclement around higher-order exceptional point (EP) singularities can provide control over higher-order modal transport, which holds promise for on-chip device applications. For future photonic technologies, controlled light steering is in demand for communication, data processing, and computing. Nonlinearity-driven dynamical encirclement of second-order EPs (EP2s) and corresponding chirality or nonchirality driven nonadiabatic modal dynamics have attracted attention in the topological study of various non-Hermitian photonic systems. Here, we propose the concept of nonlinearity-induced higher-order conjugate EPs, which are analytically associated with multiple pairs of conjugate EP2s. Moreover, in the presence of saturable nonlinearity, dynamical encirclement around higher-order conjugate EPs in two \mathcal{T} -symmetric systems are yet to be explored. Here, we report the hosting of higher-order conjugate EPs in two complementary photonic systems in the presence of nonlinearity connected with \mathcal{T} -symmetry by using the framework of a multilayer gain-loss assisted planar optical waveguide. We establish that, in the absence of chirality, the same amount of focusing and defocusing types of saturable nonlinearity leads to different dominating higher-order output modes, irrespective of the choice of the inputs, in two \mathcal{T} -symmetric devices. An analytical model to describe this anomalous higher-order mode collapsing phenomenon in two \mathcal{T} -symmetry systems owing to the interplay between nonlinearity and the topology of the higher-order conjugate EPs has been developed. Our findings provide a promising opportunity to switch higher-order modes and open up a credible platform to study the physics of nonlinearity-induced higher-order conjugate EPs in \mathcal{T} -symmetry systems.

DOI: [10.1103/PhysRevA.108.023508](https://doi.org/10.1103/PhysRevA.108.023508)

I. INTRODUCTION

The nontrivial topological nature of exceptional points (EPs) is one of the distinct non-Hermitian features of non-conservative systems [1–3], and it has also been substantially studied theoretically [4–8] as well as experimentally [9–12]. The n th-order EP (EP_n) can be defined as a specific singularity known as a branch point in the system parameter plane. It occurs when n eigenvalues and their corresponding eigenvectors converge simultaneously, resulting in a defective system Hamiltonian [1–5]. However, it has also been verified that the functionality of EP_n where $n > 2$ can be realized with the simultaneous presence of $(n - 1)$ second-order EPs [13–15]. In this paper, we conventionally use the abbreviation “ $EP_n(2, 3, 4)$ ” to define the order number of EPs. Several investigations proved that a higher-order EP has been realized by winding around appropriate numbers of connected EP2s [15–18]. The conventional Hermitian degeneracy, called the diabolic point (DP), is different from EP due to the self-adjointness of the Hamiltonian in the first and the lack of it in the second case [19].

Over the last two decades, the exotic phenomena associated with EPs were explored in many non-Hermitian systems, including optical waveguides [12,20,21], optical fiber [22], nanooptomechanical systems [23], photonic crystal [24,25],

cavity optomechanics [26], quantum heat engine [27], microcavity [28], and also in various nonoptical systems such as atomic [16] and molecular spectra [29], the cavity magnomechanical system [30], and microwave system [9,31]. However, the photonic systems which require sophisticated fabrication control can provide a highly promising platform to study the fundamental aspect of EPs as an exciting tool for manipulation of the light-matter interaction [3,32] towards a wide range of unique technological applications, such as ultrasensitive sensing [33–35], asymmetric mode switching [22,25,36–38], novel steering of fast and slow light [39], photon blockade [40], quantum switch [41], dark-state lasing [42], and coherent perfect absorption [43], nonreciprocity enhancement [44–46], optomechanically induced transparency [47], the generation of frequency components [48], phonon-lasing action [49], nonlinear EP laser [50], nonlinear phase transitions [51], enhanced stability of the nonlinear supermodes [52], and so on. A significant effort in the theoretical aspect has been put forward to investigate the higher-order EPs [6,15,16,53] instead of only second-order EPs.

An adiabatic parametric encirclement process can explore the topological nature of different-order EPs with a quasistatic variation of coupling parameters along a closed trajectory. Such a topological feature differs from the Hermitian systems, which host DPs [54]. In a Hermitian parameter-dependent Hamiltonian, the adiabatic theorem indicates that the states of the respective systems return to their initial positions apart from a global change of Berry’s phase after a slow parametric

*somiit@rediffmail.com

encirclement around a DP [55]. However, for the parameter-dependent non-Hermitian case, the adiabatic parametric encirclement around an EP2 results in the adiabatic permutation between the coupled states in the sense that two associated states successively interchange their own identities, where one of the eigenstates acquires an additional $\pm\pi$ phase change at the end of the encirclement process [19]. Such unorthodox features are indicated by the geometry of the parameter space, which is a direct consequence of the system's topology. Recently, state-switching mechanisms among multiple states were established by parametrically encircling different-order EPs [15,16,21,28]. Several experiments also [9,20,56] proved that these types of topological effects are present around EPs. These types of EP-aided state-switching mechanisms have many applications in quantum-based switching and control.

However, instead of stroboscopic encirclement around different-order EPs, if we consider time-dependent (analogous to length scale) or dynamical parametric variation around them, then the adiabaticity of the system breaks down during the evolution of the state [57]. So when we consider the clockwise and anticlockwise dynamical parametric evolution around an EP2, it results in different dominating output states, irrespective of the choice of the input state [12,20]. However, the dynamical encirclement around EP3 results in nonchiral light dynamics in the system [21,58].

The state-of-the-art facilities of fabrication in photonics give us extraordinary capabilities for fabricating complex structures to manipulate the flow of light. In seeking out new physics to exploit these capabilities, recently, the reverse chiral responses [59] in the two \mathcal{T} -symmetric devices around conjugate EP2s have opened up a new light manipulation technique in on-chip planar devices. Now, to consider a multimodal system, a natural question can be raised whether the chiral properties are maintained for higher-order conjugate EPs connecting multiple eigenstates in the presence of the other noninteracting states. Moreover, what would be the chiral aspects of the device if more than three states are mutually interacting in the vicinity of multiple pairs of conjugate EP2s in presence of judicious tuning of the parameters? In this context, the higher-order state dynamics during the dynamical parametric encirclement around higher-order conjugate EPs in the multimodal system is a contemporary issue and is yet to be explored.

Beyond the already reported reverse chiral response [59] in dual mode complementary platforms, it should be pretty exciting and more compact from a feasibility point of view in integrated devices if it is possible to switch or retrieve a selective higher-order mode in the presence of other modes with higher conversion efficiency in \mathcal{T} -symmetric devices. Hence, to host a unique nonchiral higher-order state dynamics in two \mathcal{T} -symmetric multimode but planar structures would be of interest for device applications with a deliberate choice of dynamically tunable parameters.

In this paper, to address the highlighted issue, based on the \mathcal{T} symmetry, we explore the correlation between two specially designed gain-loss-assisted multimode-supported planar complementary optical waveguides with local saturable nonlinearity to host higher-order conjugate EPs. We design a planar multimode optical waveguide (WG), where

two complementary topological variants are realized based on two \mathcal{T} -symmetric complex potentials in the form of unbalanced gain-loss profiles. Initially, by tuning the unbalanced gain-loss profile in the absence of nonlinearity, conjugate EP3s ($EP3$, $EP3^*$) were embedded by encountering two pairs of conjugate EP2s [$(EP2^{(2,5)}$, $EP2^{(2,3)})$ and $(EP2^{*(2,5)}$, $EP2^{*(2,3)})$] among three coupled modes. Instead of the reverse chiral response around conjugate EP2s [59], we show nonchiral light dynamics of the coupled chosen modes following the dynamical parametric encirclement processes, enclosing the identified conjugate EP3s. Now, with the onset of nonlinearity in the two \mathcal{T} -symmetric optical media, one of the previously unaffected modes interacts with the previously chosen three modes. Simultaneously, varying the gain-loss profile, we encounter another pair of conjugate EP2s in two complementary waveguides to connect four coupled modes analytically. We now encircle all three pairs of conjugate EP2s within the dynamical parametric loop. In this process, we establish a new type of nonchiral, higher-order modal dynamics. This exclusive dynamic is omnipresent in both the variants of complementary optical waveguides under consideration. Here, we reveal that, regardless of the choice of the input mode, all the interacting modes are collapsed into a specific dominating higher-order mode, and most interestingly, the chirality of both the complementary devices is destroyed. An analytical treatment has been developed to describe this anomalous higher-order mode-collapsing phenomenon. Even though chirality is absent around conjugate EP3s, we investigate and report the influence of saturable nonlinearity on the nonadiabatic mode conversion. The same amount of focusing (FN) and defocusing (DFN) saturable nonlinearity will lead to different dominating higher-order modes at the output of the two complementary systems. Our proposed scheme has the potential to explore an unconventional platform to investigate the higher-order nonchiral modal dynamics in two \mathcal{T} -symmetric photonic systems around higher-order conjugate EPs.

II. RESULTS AND DISCUSSIONS

A. Design of two complementary planar optical waveguides to host higher-order conjugate EPs

We design a special type of gain-loss-assisted multimodal planar optical waveguide, schematically shown in Fig. 1(a), occupying the region $-W/2 \leq x \leq W/2$ along the transverse x axis and $0 \leq z \leq L$ along the longitudinal z axis. The passive refractive index of the core (n_h) is 1.50, and the passive cladding index (n_l) is 1.46. We set the total width $W = 162\mu\text{m}$, and the full length of the waveguide as 15 mm, and set the wavelength λ in such a way that $k = 1$. Moreover, we would like to mention that, with the recent advancements in fabrication techniques, it is possible to create this type of prototype waveguide structure. Such a prototype can easily be fabricated by the thin-film deposition technique of glass material ($n_h = 1.5$) over a thick silica glass ($n_l = 1.46$) substrate. Our passive waveguide supports six linearly polarized quasiguided optical modes, i.e., $\psi_i (i = 1, 2, 3, 4, 5, 6)$. The chosen input field intensities of

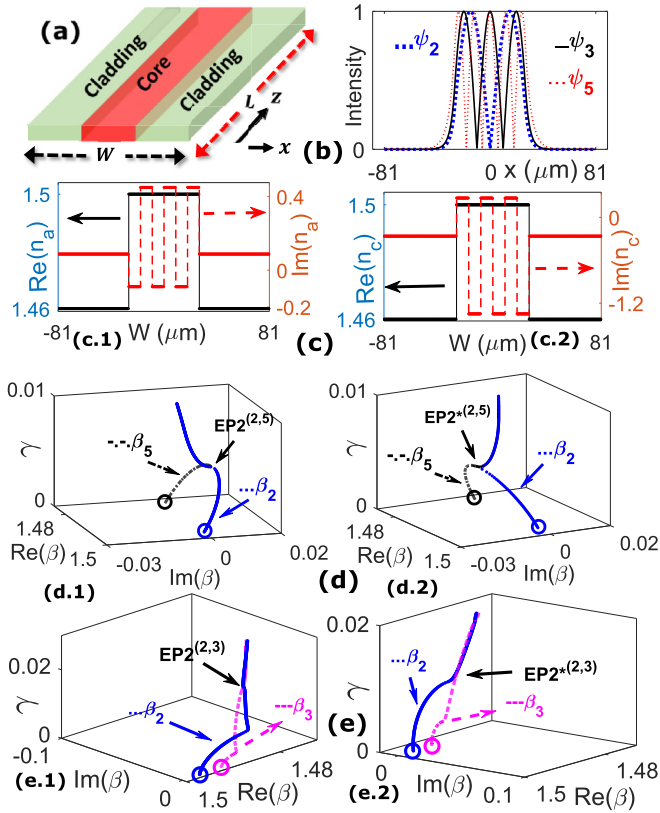


FIG. 1. (a) Schematic diagram of the proposed gain-loss-assisted planar waveguide to realize two \mathcal{T} -symmetric complementary variants, having width W (along the transverse x axis) and optimized length L (along the propagation axis z). (b) Normalized field intensity profile of three chosen modes $\psi_j(2, 3, 5)$. The blue square dotted line indicates ψ_2 , the solid black line represents ψ_3 , and the dotted red line symbolizes ψ_5 . (c) Complex transverse refractive index profiles of two complementary variants, whereas (c.1) represent for n_a and (c.2) represents for n_c . The black line represents the variation of real part of the refractive index profile $\text{Re}(n)$ and red dotted line represent their respective imaginary part of the refractive index $\text{Im}(n)$ variation for a specific cross section of the waveguide associated with $\gamma = 0.0043$ and $\tau = 5$. (d) Coalescence of complex β 's (dotted blue and dashed dotted black curve represent for β_2 and β_5 , respectively) simultaneously at $\gamma = 0.0043$ for a chosen $\tau = 5$. (d.1) and (d.2) Indicates the location of two conjugate EP2s ($[EP2^{(2,5)}, EP2^*(2, 5)]$) in two complementary WGs, respectively. (e) Coalescence of complex β_2 and β_3 (dotted blue and dashed pink curve, respectively) at $\gamma = 0.018$ for a chosen $\tau = 1.85$. Panels (e.1) and (e.2) indicate the location of an other pair of conjugate EP2 ($[EP2^{(2,3)}, EP2^*(2, 3)]$) in two complementary WGs, respectively

three modes $\psi_j(j = 2, 3, 5)$ supported by the passive WG are shown in Fig. 1(b). Here, the non-Hermiticity is introduced by a specific transverse distribution of a multilayer gain-loss profile, controlled by two tunable parameters as γ to represent the gain coefficient and τ to define a fixed loss-to-gain ratio. Now we consider two complementary waveguide variants (WG_a and WG_c) concerning the \mathcal{T} -symmetry complex potentials in such a way that the refractive index profile of the respective variants [i.e., $n_a(x)$ and $n_c(x)$, respectively] can be

written as

$$n_a(x) = \begin{cases} n_l + i\gamma, & \text{for cladding } W/6 \leq |x| \leq W/2, \\ n_h - i\gamma, & \text{for core } \begin{cases} -W/6 \leq x \leq -W/9, \\ W/18 \leq x \leq 0, \\ W/18 \leq x \leq W/9, \end{cases} \\ n_h + i\tau\gamma, & \text{for core } \begin{cases} -W/9 \leq x \leq -W/18, \\ 0 \leq x \leq W/18, \\ W/9 \leq x \leq W/6, \end{cases} \end{cases} \quad (1)$$

and

$$n_c(x) = \begin{cases} n_l - i\gamma, & \text{for cladding } W/6 \leq |x| \leq W/2, \\ n_h + i\gamma, & \text{for core } \begin{cases} -W/6 \leq x \leq -W/9, \\ -W/18 \leq x \leq 0, \\ W/18 \leq x \leq W/9, \end{cases} \\ n_h - i\tau\gamma, & \text{for core } \begin{cases} -W/9 \leq x \leq -W/18, \\ 0 \leq x \leq W/18, \\ W/9 \leq x \leq W/6. \end{cases} \end{cases} \quad (2)$$

In the core region ($-W/6 \leq x \leq W/6$), there are six alternate gain-loss layers with equal width, whereas cladding ($-W/6 \leq |x| \leq W/2$) consists of either loss or gain depending on the respective complementary variants. The overall transverse profiles of $n_a(x)$ and $n_c(x)$ are shown in Fig. 1(c), where the solid black line (in the left y axis) and the dotted red line (in the right y axis) indicates real [$\text{Re}(n)$] and imaginary [$\text{Im}(n)$] part of the refractive index profiles (for a specific $\gamma = 0.0043$ and $\tau = 5$), respectively. So, it clearly indicates in Figs. 1(c.1) and 1(c.2) that, owing to \mathcal{T} symmetry, two complementary waveguides experience exactly opposite gain-loss variation along the transverse x axis. Here, gain-loss distribution is associated with the specific set of a (γ, τ) for each cross section of the two proposed complementary systems. Now, we can control the interaction among the modes by varying the coupling parameters (γ, τ) along the propagation directions.

Higher-order conjugate EPs have been embedded in both complementary WGs by encountering multiple pairs of connecting conjugate EP2s among the chosen modes. We found multiple conjugate EP2s in two complementary WGs among the specifically chosen propagation constants of the modes by topological ARC-type interactions [5,28] by solving the scalar modal equations. We compute the propagation constants of the modes using the scalar modal equation [according to the instantaneous modes profile $\psi(x)$], which is given by

$$[\partial_x^2 + n^2(x)\omega^2 - \beta^2]\psi(x) = 0. \quad (3)$$

Even though the waveguide supports six quasiguided modes, we can choose different sets of coupled modes to encounter higher-order conjugate EPs by appropriate settings of the gain-loss profile. In the absence of nonlinearity but with proper tuning of (γ, τ) , $EP3$ and $EP3^*$ are embedded by encountering two distinct pairs of connecting conjugate EP2s among three chosen modes in two complementary WGs,

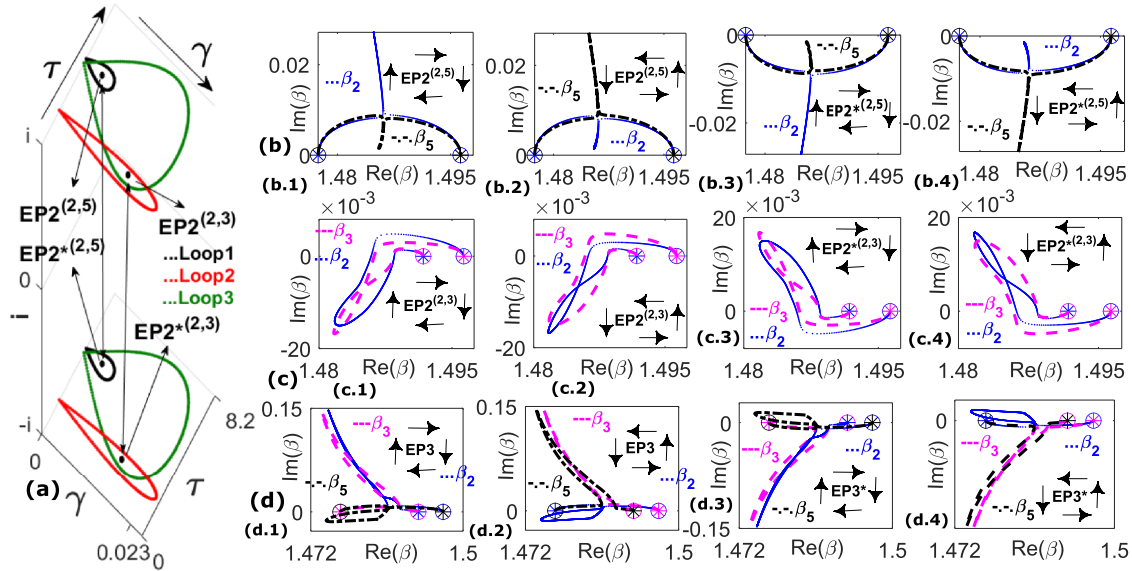


FIG. 2. (a) Three chosen parametric loops in (γ, τ) plane to encircle identified pairs of conjugate EP2s [following Eq. (4)] associated with \mathcal{T} -symmetry complementary variants (as shown with respect to an additional i axis), where Loop1 (smallest area black dotted curve) and Loop2 (medium area red dotted curve) encircle two distinct conjugate pairs ($EP2^{(2,5)}$, $EP2^{*(2,5)}$) and ($EP2^{(2,3)}$, $EP2^{*(2,3)}$), respectively, and Loop3 (largest area green dotted curve) encircles both the identified pairs of conjugate EP2s simultaneously. (b) Adiabatic switching between β_2 (dotted blue) and β_5 (dashed dotted black) due to individual parametric encirclement of $EP2^{(2,5)}$ and $EP2^{*(2,5)}$ in CW and CCW direction by Loop1, unaffected β_3 (dashed pink). (c) Similar adiabatic switching between β_2 (dotted blue) and β_3 (dashed pink) due to individual parametric encirclement of $EP2^{(2,3)}$ and $EP2^{*(2,3)}$ in CW and CCW direction by Loop2, unaffected β_5 (dashed dotted black). (d) Third-order adiabatic switching phenomenon among β_2 , β_3 , and β_5 in the complex β plane, following simultaneous encirclement (as Loop3) of both the EP2s ($EP2^{(2,5)}$, $EP2^{(2,3)}$) and their conjugate counterparts ($EP2^{*(2,5)}$, $EP2^{*(2,3)}$) in both CW and CCW directions.

respectively. For a specific value of $\tau = 5$, it is observed in Fig. 1(d) that β_2 and β_5 coalesce at $\gamma = 0.0043$, referring to the presence of EP2 at ($\gamma = 0.0043$, $\tau = 5$), for both the complementary variants. In Fig. 1(d.1), the coalescence is observed along the positive Im -axis for WG_a as it is loss-dominated. However, in Fig. 1(d.2), it is observed that the coalescence is observed along the negative Im axis for WG_c as it is gain-dominated. Thus, in the same passive waveguide, based on the \mathcal{T} -symmetry gain-loss profile, we encounter two EP2s in the (γ, τ) plane. These two EP2s can conventionally be defined as second-order conjugate EPs (say $EP2^{(2,5)}$ and $EP2^{*(2,5)}$) in their respective (γ, τ) spaces, which are associated with two complex conjugate $\text{Im}(n)$ profiles of corresponding two complementary structures (WG_a and WG_c , respectively) of the designed passive WG. Similarly in Fig. 1(e), by properly tuning the gain-loss profile, we find another pair of conjugate EP2s between β_2 and β_3 in two complementary variants, such as $EP2^{(2,3)}$ and $EP2^{*(2,3)}$ at (0.018, 1.85). In Fig. 1(e.1), we show that the coalescence observed along negative Im axis for WG_a as it is gain-dominated; however, in Fig. 1(e.2), coalescence observed along the positive Im axis for WG_c as it is loss-dominated. So, in both the cases, the locations of $EP2^{(2,3)}$ and $EP2^{*(2,3)}$ are the same but conjugate in nature.

B. Adiabatic modal dynamics: Encounter of higher-order conjugate EPs

Here, we investigate the branch-point behavior during quasistatic parametric encirclement processes around the dif-

ferent identified pairs of conjugate EP2s in the (γ, τ) plane associated with complementary WGs. To meet the device implementation requirement, we chose the shape of the parameter space in such a way that both the beginning and end of the encirclement process reach at $\gamma = 0$ [22,25,28,57]. To ensure such a condition, we implement the parametric equations

$$\gamma(\phi) = \gamma_0 \sin(\phi/2), \quad \tau(\phi) = \tau_0 + r \sin(\phi) \quad (4)$$

to enclose single or multiple pairs of conjugate EP2s (with $\gamma_0 > \gamma_{EP}$), as shown in Fig. 2(a). Here, γ_0 , τ_0 , and r are three characteristic parameters and the tunable angle ϕ ($0 \leq \phi \leq 2\pi$) by which we can encircle specific EP2 in their respective (γ, τ) plane. In Fig. 2(a), $\gamma_{EP}(=0.0043)$ and $\tau_{EP}(=5)$ we define the location of $EP2^{(2,5)}$ and $EP2^{*(2,5)}$ (enclosing by Loop1; $\gamma_0 = 0.007$, $\tau_0 = 5$, $r = 0.5$) with respect to the additional i axis [$+i$ indicates WG_a and $-i$ for WG_c]. Whereas $\gamma_{EP}(=0.0185)$ and $\tau_0(=1.85)$ define the location of $EP2^{(2,3)}$ and $EP2^{*(2,3)}$ (enclosing by Loop2; $\gamma_0 = 0.02$, $\tau_0 = 1.85$, $r = 0.5$) with respect to the same i axis. Now we consider a new parametric loop (say Loop3; $\gamma_0 = 0.024$, $\tau_0 = 4.75$, $r = 3$) to encircle both pairs of conjugate EP2s simultaneously.

Now we track the trajectories of complex β_j ($j = 2, 3, 5$) in Figs. 2(b), 2(c), and 2(d) following the stroboscopic variation of γ and τ along the chosen three loops [by using Eq. (4)]. In Figs. 2(b.1) and 2(b.3) we show the trajectories for encirclement of $EP2^{(2,5)}$ and $EP2^{*(2,5)}$ in the clockwise (CW) way ($\phi : 0 \rightarrow 2\pi$), respectively. However, in Figs. 2(b.2) and 2(b.4), we show the trajectories for the encirclement of $EP2^{(2,5)}$ and $EP2^{*(2,5)}$ in the anticlockwise (CCW) direction ($\phi : 2\pi \rightarrow 0$), respectively. In both cases, we also observe

that the trajectory of β_3 regains its initial position, so it is unaffected. The hosting of such conjugate EP2 encirclement schemes in two \mathcal{T} -symmetric systems of the designed optical WG indicates adiabatic exchange between the initial positions of the connecting β_2 (blue curve) and β_5 (black curve) in the complex β space, as is shown in Fig. 2(b), which reveals the second-order branch-point behavior of the pair of conjugate EP2. Here, it is observed that the overall β trajectories due to the encirclement of EP2^(2,5) and EP2*^(2,5) in any of the particular directions look like two perfect mirror images with respect to the $\text{Im}(\beta)$ axis. Similarly, another trajectory between β_2 (blue curve) and β_3 (pink curve) is shown in Fig. 2(c), while varying the parameter space along the Loop2, which encircles another pair of conjugate EP2 (say, EP2^(2,3) and EP2*^(2,3)). Here, the adiabatic exchange is observed between β_2 (blue curve) and β_3 (pink curve) at the end of the encirclement process, and they are also analytically connected through this conjugate EP2 pair. In this case, β_5 is not connected through this pair, so it remains uninteracted. Here, it is also noticeable that the overall β_2 and β_3 trajectories due to this pair of conjugate EP2 encirclement in any of the specific directions look like exact mirror images with respect to the $\text{Im}(\beta)$ axis. Now, to consider the third-order mode exchange phenomenon, we choose another loop [Loop3; as shown in Fig. 2(a)], which encircles two identified pairs of conjugate EP2s, simultaneously. In this case, we track the trajectories of β_j ($j = 2, 3, 5$) in Fig. 2(d). Here with the quasistatic parametric variations in any of the specific encirclement directions (CW or CCW) along the Loop3, all three chosen propagation constants ($\beta_2, \beta_3, \beta_5$) of the coupled modes exchange their own identities for making a complete loop following the CW encirclement: $\beta_2 \rightarrow \beta_3 \rightarrow \beta_5 \rightarrow \beta_2$ in a complex β plane. Thus, the system shows third-order branch-point behavior for the corresponding eigenvalues if both the identified pairs of conjugate EP2s are quasistatically encircled in (γ, τ) space, simultaneously. This occurrence of successive adiabatic state exchange around pairs of conjugate EP2s certainly validates the emergence of a conjugate EP3. It appears within two complementary system parameter spaces, where all three selected modes are analytically intertwined. Here, we observed that the trajectories of third-order β switching due to encirclement around EP3 and EP3* in any of the specific directions look like two mirror images with respect to the $\text{Im}(\beta)$. We also observe that, if we reverse the parametric encirclement direction, then the chosen complex β values exchange successively as $\beta_2 \rightarrow \beta_5 \rightarrow \beta_3 \rightarrow \beta_2$ in the complex β plane, which are exactly the opposite progressions from the previous observation. To control the interaction among the supported modes, in addition with the optical gain-loss, we introduce local saturable nonlinearity having the form

$$\Delta n_{\text{NL}}(x, z) = \sigma \frac{n_2 |\psi|^2}{[1 + (|\psi|^2/I_s)]}, \quad (5)$$

where n_2 represents the nonlinear coefficient and I_s is the saturating intensity. Here, $\sigma = +1$ (-1) for focusing (defocusing) nonlinearity. Unlike Kerr-type nonlinearity, we deliberately incorporate the saturable nonlinearity to avoid any instability in higher-order modal output. However, this type of nonlinearity variation is saturated by the appropriate choice of I_s after

propagating for a sufficient length. Here the actual nonlinearity level is quantified in the form of $(\Delta n_{\text{NL}}/\Delta n) \times 100\%$ with $\Delta n = (n_h - n_l)$. Here, we can achieve different amounts of nonlinearities by adjusting the input signal power with the proper choice of n_2 .

C. Dynamical parametric encirclement: Beam propagation dynamics around conjugate EP3 in the absence of nonlinearity

After encountering two distinct pairs of conjugate EP2s, we identify the adiabatic mode exchange phenomena. This identification occurs due to the quasistatic encirclement of the coupling parameters around these points. This observation follows the principles outlined in the adiabatic theorem discussed in the previous section. To investigate the propagation of the quasiguided modes through the two complementary \mathcal{T} -symmetric variants of the designed optical waveguide, we map the parameter loops associated with different conjugate EP2s throughout the length of the waveguide. If we consider dynamical parametric encirclement (time-dependent parametric distribution), the inversion symmetry gets broken in the overall gain-loss variation along the timescale, which competes with the adiabatic theorem [57]. A complete encirclement process ($\phi : 0 \rightarrow 2\pi$) followed by such a dynamical encirclement method is equivalent to one complete pass of light through the WG ($z : 0 \rightarrow L$). Here, the control parameters vary along the length or analogous time for the optical system (to establish the equivalence of the Helmholtz equation with Schrödinger equation). We utilize the concept of \mathcal{T} symmetry, which allows for the transformation of t to $-t$. By analogy, we map the parameter space along the length or the z axis in two opposite directions. This is done for the two variants of the waveguide, which exhibit \mathcal{T} symmetry. However, at each transverse cross section (at fixed z), the refractive index profiles for two complementary systems correspond to a specific set of (γ, τ) . Accordingly, such a parameter space mapping is implemented by the consideration of

$$\phi = \left[\frac{2\pi z}{L} \right] \quad \text{and} \quad \phi = \left[\frac{2\pi(L-z)}{L} \right] \quad (6)$$

separately in Eq. (4) to realize the dynamical encirclement of different pairs of conjugate EP2s. The following modified parameter space for WG_a as

$$\gamma(z) = \gamma_0 \sin \left[\frac{\pi z}{L} \right]; \quad \tau(z) = \tau_0 + r \sin \left[\frac{2\pi z}{L} \right]. \quad (7)$$

Here, CW encirclement is implemented by the propagation of light from $z = 0$ to L and CCW encirclement is associated with the propagation from opposite end, i.e., from $z = L$ to $z = 0$, respectively. Similarly, the modified parameter space for WG_c is

$$\gamma(z) = \gamma_0 \sin \left[\frac{\pi(L-z)}{L} \right], \quad \tau(z) = \tau_0 + r \sin \left[\frac{2\pi(L-z)}{L} \right]. \quad (8)$$

In this case, $z = 0$ and $z = L$ are associated with $\phi = 2\pi$ and 0, respectively. We can achieve the required longitudinal gain-loss profile by using either a standard photolithography

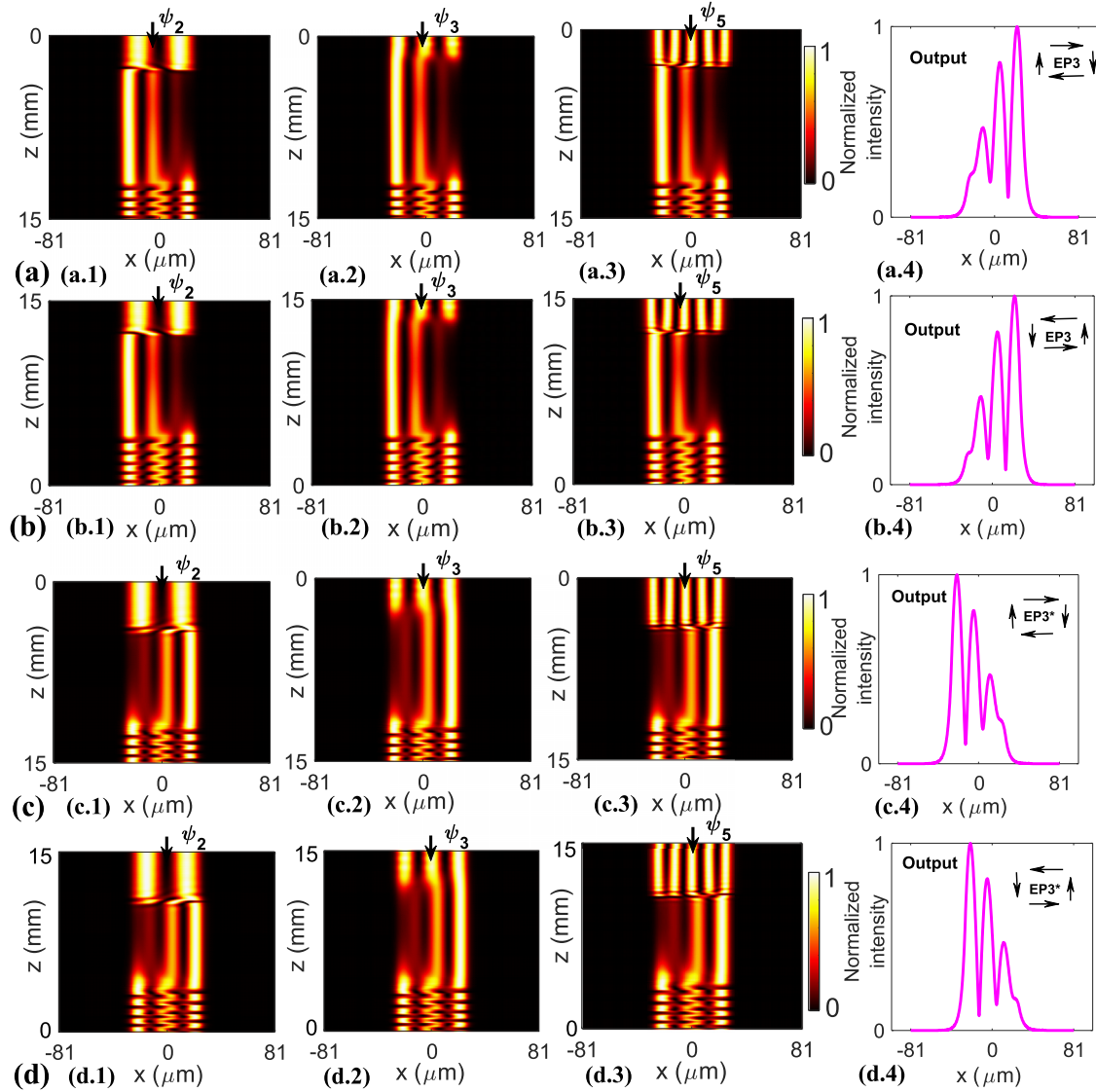


FIG. 3. (a) Beam propagation simulation results for the CW dynamical encirclement around $EP2^{(2,5)}$, $EP2^{(2,3)}$, simultaneously [conversion of $(\psi_2, \psi_3, \psi_5) \rightarrow \psi_3$] through WG_a , and (b) for CCW direction, showing the similar conversion in WG_a . (a.4), (b.4) show the output field intensities at $z = L$ and $z = 0$, respectively associated with the conversion through WG_a . (c), (d) Beam propagation simulation results through WG_c for the dynamical encirclement around $EP2^{*(2,5)}$, $EP2^{*(2,3)}$, together [conversion of $(\psi_2, \psi_3, \psi_5) \rightarrow \psi_3$], in (c) the CW direction and (d) the CCW direction. (c.4), (d.4) the output field intensities at $z = L$ and $z = 0$, respectively, associated with the conversion through WG_c .

technique or controlled doping of active or lossy materials with state-of-the-art fabrication techniques.

Here, we investigate the light dynamics around conjugate EP3s in the presence of two different pairs of conjugate EP2s in two complementary systems as per Eqs. (7) and (8). If we consider any single pair of conjugate EP2 [($EP2^{(2,5)}$ and $EP2^{*(2,5)}$) or ($EP2^{(2,3)}$ and $EP2^{*(2,3)}$)] and study the light dynamics around it, we observe the reverse-chiral response of two complementary waveguides with respect to the direction of the encirclement process. The individual dynamical encirclements around conjugate EP2 in opposite directions results in the delivery of the same dominating modes by their respective waveguide variants. However, the section on the reverse chiral response around any single pair of conjugate EP2s in two complementary systems is deliberately not included in the paper, as it has already been reported [59]. Here,

we show that, due to the dynamical encirclement around the conjugate EP3 associated with two complementary systems, all the interacting modes associated with it get converted into a specific higher-order mode, irrespective of the choice of the input direction. We thoroughly investigate the intriguing physics of the conjugate EP3 and explore the resulting light dynamics in their vicinity, as shown in Fig. 3. For a sufficiently slow variation of $\text{Im}(n)$ within the adiabatic limit along the z direction, the dynamics of quasiguided modes are governed by the (1+1)D scalar beam propagation equation (under paraxial approximation) as

$$2i\omega \frac{\partial \psi(x, z)}{\partial z} = - \left[\frac{\partial^2}{\partial x^2} + \Delta n^2(x, z) \omega^2 \right] \psi(x, z), \quad (9)$$

where $\Delta n^2(x, z) \equiv n^2(x, z) - n_l^2$. We use the split steps Fourier method to solve Eq. (9) [60]. It was established that,

during the dynamical encirclement process, one of the coupled modes evolves with lower average loss following the adiabatic expectations followed by the associated β trajectories [25]. In Figs. 3(a) and 3(b), we show the beam propagation simulation results in WG_a for the dynamical encirclement process along Loop3, which encloses $EP2^{(2,5)}$ and $EP2^{(2,3)}$ (or equivalent to an $EP3$) simultaneously. Here, in Fig. 3(a), to consider CW encirclement, we choose the input port at $z = 0$ to launch the input. Here, all three coupled modes (ψ_2, ψ_3, ψ_5) associated with $EP2^{(2,5)}$, $EP2^{(2,3)}$ are converted into ψ_3 at $z = L$ beyond the adiabatic expectation unlike the corresponding β trajectories, as shown in Fig. 2(d.1). Here, β_5 evolves with lower average loss in comparison to β_2 and β_3 , so the respective mode ψ_5 is adiabatically converted to ψ_3 , but the other two modes (i.e., ψ_2 and ψ_3) experience nonadiabatic transitions (NAT). Now, if we consider CCW encirclement around $EP3$, all the analytically connected modes are converted to ψ_3 , irrespective of the choice of the input modes. However, in this case, ψ_2 evolves adiabatically due to lower average loss and the two other modes follow NAT.

Now, we consider checking the effect of dynamical encirclement around $EP3^*$ in WG_c . In Figs. 3(c) and 3(d), for CW and CCW encirclements around $EP3^*$ (associated with simultaneous encirclement around $EP2^{*(2,5)}$ and $EP2^{*(2,3)}$), all the chosen coupled modes are converted into ψ_3 at the end of the encirclement process. However, here, for CW and CCW encirclements, β_2 and β_5 evolve adiabatically due to lower average loss, respectively, which is exactly the opposite from the previous encirclement process, as shown in Figs. 3(a) 3(b). Thus, owing to the breakdown of the adiabaticity during evolutions of the interacting modes, the nonchiral dynamics is evident for the dynamical encirclement scheme around conjugate $EP3$ in two \mathcal{T} -symmetric WGs. Here, we introduced the term “nonchiral” in the general sense, which refers to the property of two complementary systems that exhibit the same outputs, regardless of the direction of the input.

We also calculate the conversion efficiencies in terms of the overlap integral as

$$C_{P \rightarrow Q} = \frac{|\int \psi_P \psi_Q dx|^2}{\int |\psi_P|^2 dx \int |\psi_Q|^2 dx}, \quad \{P, Q\} \in i. \quad (10)$$

Here, $C_{P \rightarrow Q}$ defines the conversion efficiency for the conversion $\psi_P \rightarrow \psi_Q$. The maximum conversion efficiencies for CW and CCW encirclements (associated with dynamical encirclement around $EP3$) in WG_a are 77% and 72%, respectively. On the other hand, the conversions $\{\psi_2, \psi_3, \psi_5\} \rightarrow \psi_3$ in WG_c for CW and CCW directions (associated with dynamical encirclement around $EP3^*$) are 73% and 75%, respectively.

D. Dynamical parametric encirclement: Nonchiral beam propagation dynamics in the presence of nonlinearity

The above investigations were carried out in the absence of any local nonlinearity when three interacting modes were associated with conjugate $EP3$ with the simultaneous presence of other noninteracting modes. Now, we introduce the effect of intensity-dependent saturable nonlinearity in the spatial index distribution and further investigate the dynamics of interacting modes. Here, by introducing the nonlinearity, the

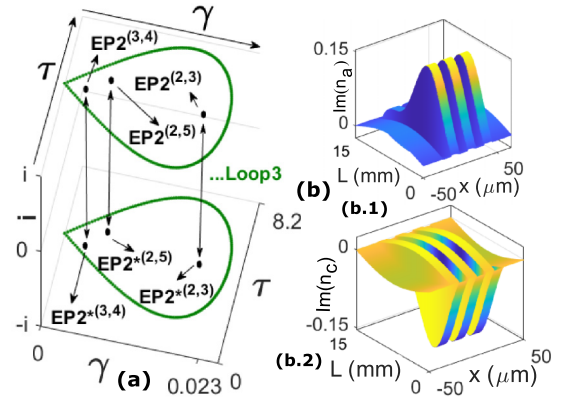


FIG. 4. (a) Parametric loops in the (γ, τ) plane to encircle three identified pairs of conjugate EP2s, simultaneously. (b) The overall length dependent variations of $\text{Im}(n_a)$ and $\text{Im}(n_c)$ associated with \mathcal{T} -symmetric complementary waveguides [(b.1) for WG_a and (b.2) for WG_c , respectively] after mapping the respective (γ, τ) -parameter spaces to dynamically encircle all the identified EP2s and their conjugate parts, respectively.

real refractive index profile is locally modified, and due to that, the complex β values also get modified. We investigate the light dynamics through the two complementary variants for various nonlinearity strengths by changing the input intensity levels. Here, we observe that, for the nonlinearity level up to 2.5%, the proposed complementary variants possess a similar kind of beam dynamics, as shown in Fig. 3. However, once we reach the nonlinearity level 3.2% in the two \mathcal{T} -symmetric variants, the corresponding local modification of $n(x)$ sufficiently affects the dynamics of ψ_4 , and then it starts interacting with the other three chosen modes (ψ_2, ψ_3, ψ_5). Such types of mutual interactions remain intact up to a strength of 9% nonlinearity. Thus, by changing the nonlinearity percentage within this range (3.2% \rightarrow 9%), we can control the simultaneous interactions among four modes in both the complementary WGs. We choose a specific signal intensity to introduce 4.2% nonlinearity in the special index distribution of the two complementary WGs and observe the mutual interactions among all the modes to host multiple conjugate EP2s. Here, investigating the ARCs between the different pairs of $\beta_j (j = 2, 3, 4, 5)$ in the presence of nonlinearity, we encounter another pair of conjugate EP2 (say: $EP2^{(3,4)}$, $EP2^{*(3,4)}$) in the (γ, τ) plane at location (0.0022, 3.25) in addition to the other two pairs of conjugate EP2s (as demonstrated previously). So the simultaneous presence of three pairs of conjugate EP2s analytically connects four quasiguided modes $\psi_j (2, 3, 4, 5)$. We dynamically encircle all three pairs of conjugate EP2s simultaneously using the length-dependent parametric loop shown in Fig. 4(a) and perform the beam propagation dynamics. The corresponding $\text{Im}[n(x, z)]$ distributions for CW dynamical encirclement in two complementary variants are shown in Fig. 4(b), where Fig. 4(b.1) is for WG_a and Fig. 4(b.2) corresponds to WG_c . We chose the size of the parameter loop in such a way that the presence of a certain level of nonlinearity does not affect the location of the other pairs of EP2s. By introducing up to a specific level of nonlinearity (ranging from 3.2% to 9%) in

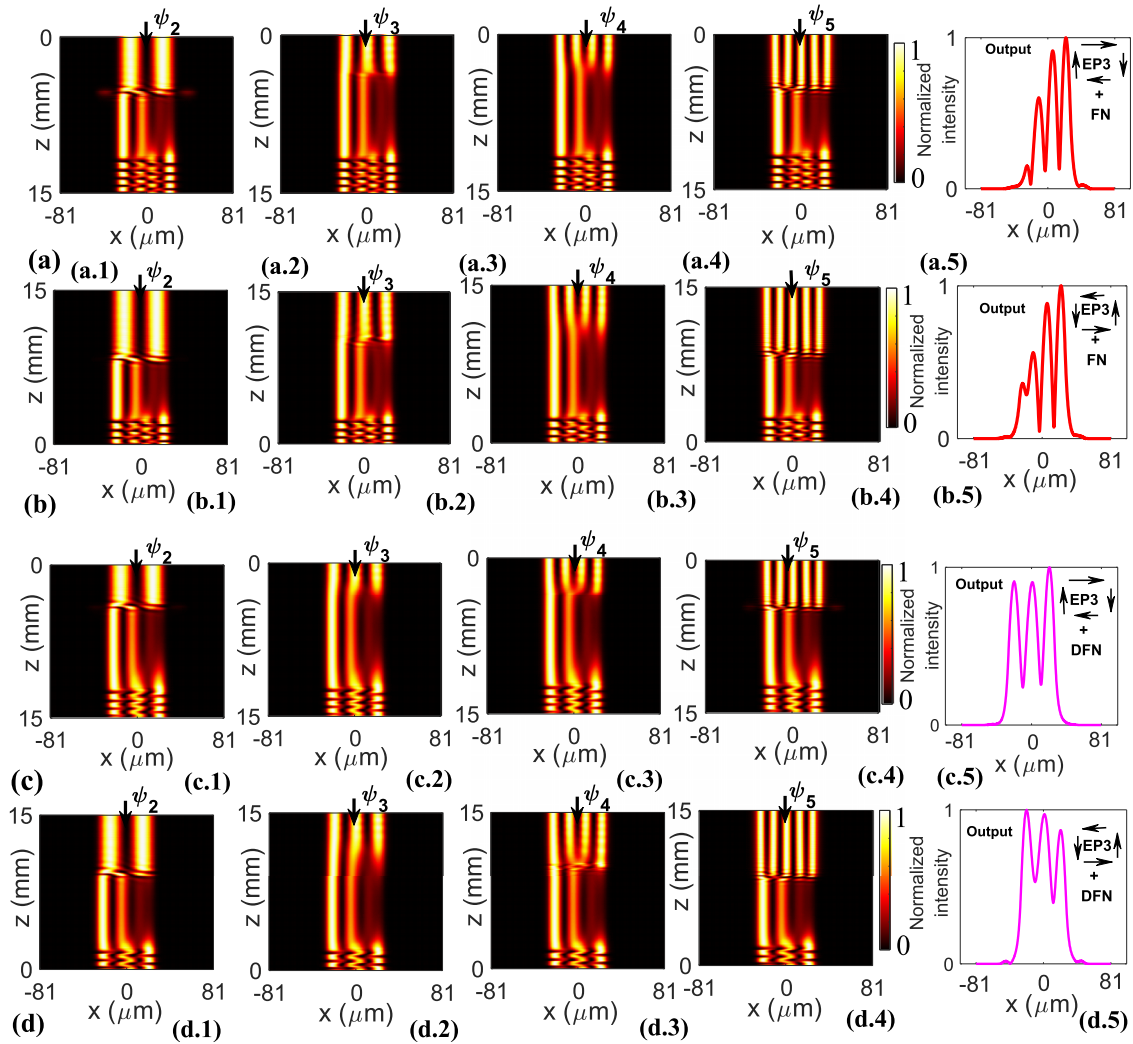


FIG. 5. (a), (b) Beam propagation simulation results through WG_a in presence of focusing nonlinearity (FN), the conversion of $[(\psi_2, \psi_3, \psi_4, \psi_5) \rightarrow \psi_4]$ following dynamical encirclement around three identified EP2s [$EP2^{(2,5)}$, $EP2^{(2,3)}$, $EP2^{(3,4)}$] in CW, CCW directions, respectively, where all the interacting modes collapsed to ψ_4 . (a.5) and (b.5) Output field intensities in the presence of FN at $z = L$ and $z = 0$, respectively, associated with the conversion through WG_a . (c), (d) Beam propagation simulation results through WG_a in the presence of defocusing nonlinearity (DFN): in the presence of DFN in the optical medium for both CW and CCW encirclement direction, all the interacting modes are collapsed into ψ_3 . (c.5) and (d.5) Output field intensities in the presence of DFN at $z = L$ and $z = 0$, while three identified EP2s are encircled in CW and CCW directions, respectively.

the parameter loops, it is possible to ensure that all the anticircled positions of the EP2s are encompassed within the loops. Essentially, we design the topologically complementary structures in such a way that we can consider both cases, i.e., with and without nonlinearity. Now, if we choose $\sigma = 1$ to consider FN in the WG_a variant, the light propagation due to dynamical encirclement along Loop3 [indicated in Fig. 4(b.1); associated with $EP2^{(3,4)}$, $EP2^{(2,5)}$, and $EP2^{(2,3)}$] are shown in Figs. 5(a) and 5(b). In Fig. 5(a), it is evident that all the four coupled modes are collapsed into ψ_4 (light propagation in the forward direction, i.e., from $z = 0$ to $z = L$), given that, due to lower average loss, ψ_5 evolves adiabatically and the other three modes (ψ_2, ψ_3, ψ_4) evolve nonadiabatically. Now, instead of forward light propagation, if we reverse the propagation direction, i.e., from $z = L$ to $z = 0$, we get similar modal dynamics as can be seen in Fig. 5(b). In this case, ψ_3 evolves adiabatically and the other three modes follow NAT. We also

calculated the conversion efficiencies followed by Eq. (10). In this case, the maximum conversion efficiencies for CW and CCW encirclements are 95% and 98%, respectively. Now, we consider the same amount of DFN ($\sigma = -1$) and study the beam propagation dynamics of the chosen coupled modes in Figs. 5(c) and 5(d) for CW and CCW encirclement along the same parametric loop described in Fig. 4(b.1). As can be seen here, for both the encirclement direction, four interacting modes are collapsed in ψ_3 at the output end of the WG_a . Moreover, in this case, the maximum conversion efficiencies for CW and CCW encirclements are 96% and 97%, respectively. So, it is clearly observed that conversion efficiencies have increased drastically after applying a certain percentage of nonlinearity. A comparative study of the output field intensities has been done at different nonlinearity conditions in WG_a . Figures 5(a.5) and 5(b.5) represent the normalized output intensities for CW and CCW encirclement conditions

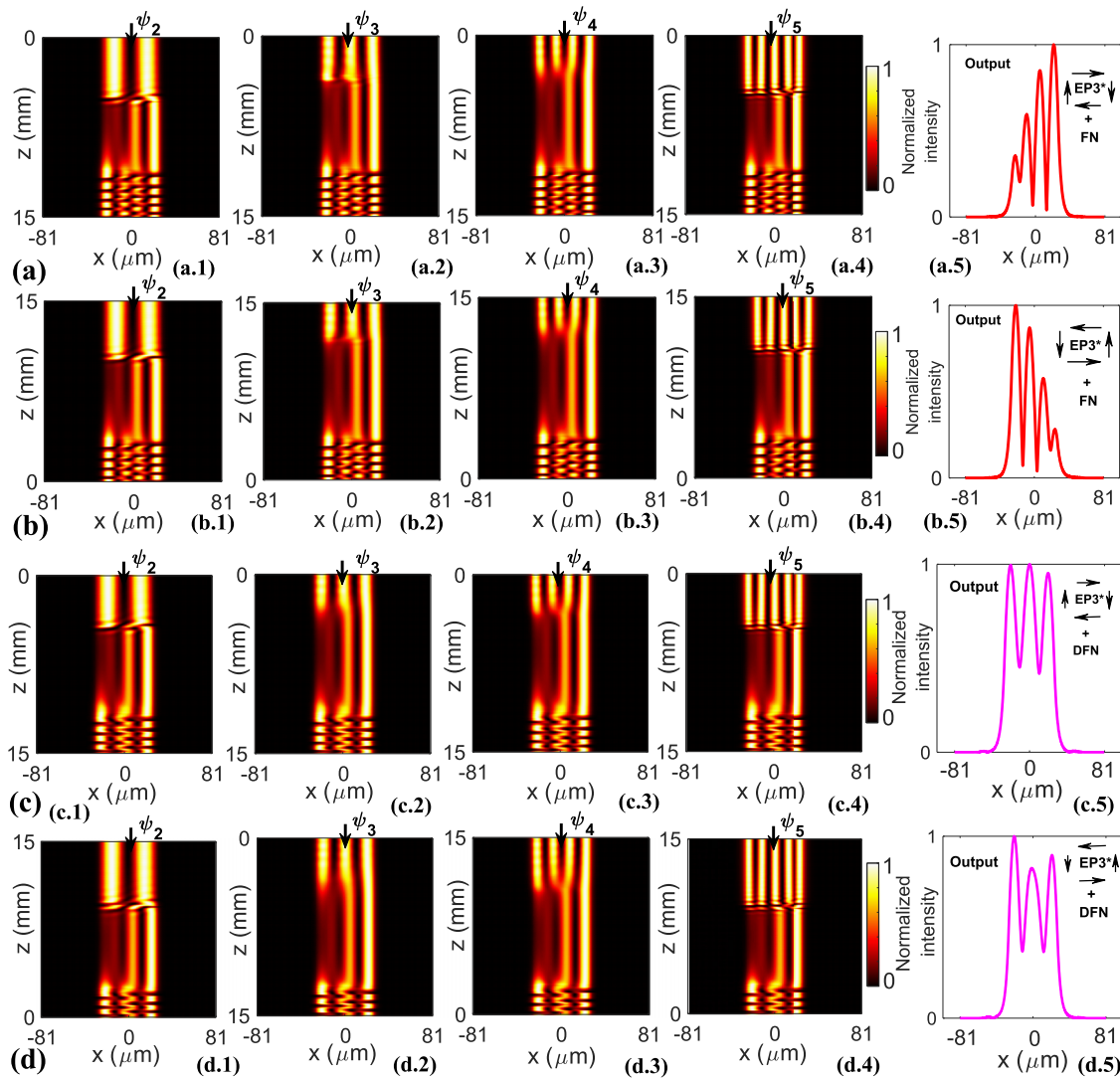


FIG. 6. (a) Beam propagation simulation results through WG_c in presence of FN, the conversion of $[(\psi_2, \psi_3, \psi_4, \psi_5) \rightarrow \psi_4]$ following dynamical encirclement around three identified EP2s [$EP2^{(2,5)}$, $EP2^{(2,3)}$, $EP2^{(3,4)}$] in CW, CCW directions, respectively, where all the interacting modes collapse to ψ_4 . (a.5) and (b.5) Output field intensities in the presence of FN at $z = L$ and $z = 0$, respectively associated with the conversion through WG_c . (c), (d) Beam propagation simulation results through WG_c in the presence of DFN: however, in the presence of DFN in the optical medium for both CW and CCW encirclement directions, all the interacting modes are collapsed into ψ_3 . (c.5) and (d.5) Output field intensities in the presence of DFN at $z = L$ and $z = 0$, while three identified EP2s are encircled in CW and CCW directions, respectively.

in the presence of FN, respectively, whereas Figs. 5(c.5) and 5(d.5) show the same for both the encirclement conditions in the presence of DFN, respectively. Now, if we choose another complementary structure WG_c , and select $\sigma = 1(-1)$ to consider FN (DFN), the corresponding beam propagation dynamics are shown in Fig. 6. Here, for introducing 4.2% of FN, the beam propagation dynamics due to CW and CCW dynamical encirclement along the same loop [in Fig. 4(b.2); associated with $EP2^{*(3,4)}$, $EP2^{*(2,5)}$ and $EP2^{*(2,3)}$] are shown in Figs. 6(a) and 6(b), respectively. In this case, the coupled four modes collapse into ψ_4 at the output end, irrespective of the choice of the input direction. Here, we observe that ψ_2 evolves adiabatically for CW encirclement, while ψ_5 evolves adiabatically for CCW encirclement. Similarly, for considering the same amount of DFN, four coupled modes collapse into ψ_3 due to CW and CCW dynamical encirclement around Loop3, which are shown in Figs. 6(c) and 6(d). Here, we

observe that ψ_2 evolves adiabatically for CW encirclement, while ψ_4 evolves adiabatically for CCW encirclement. This adiabatic evolution is attributed to the lower average losses of the respective modes during parametric encirclement.

However, if we further increase the nonlinearity level (above 9%), then, due to the overall modification of the index profile, conjugate pairs of EP2s may not be appropriately encircled, and the overall light dynamics may be taken over by the effect of nonlinearity. In this context, instead of using nonlinearity to manipulate the higher-order conjugate EPs (associated with multiple pairs of connecting EP2s) positions, it can also be possible to control the locations by changing the real refractive index of the waveguide. However, dynamically changing the refractive index profile in any two complementary waveguide variants is challenging during device applications. So we deliberately use a certain percentage of nonlinearity as a tuning parameter for dynamic refractive

index modification. The proposed prototype design can be effectively implemented using appropriate fabrication techniques while ensuring proper scalability to select the suitable nonlinearity level. So the mode-collapsing phenomenon is a result of the interplay between the topology of exceptional points (EPs) and nonlinearity along the dynamical loop that encircles multiple pairs of conjugate EP2s, as shown in Figs. 5 and 6.

III. ANALYTICAL TREATMENT FOR NONLINEARITY-INDUCED LIGHT DYNAMICS

Here a detailed analytical treatment based on nonadiabatic correction factors is presented to establish the anomalous higher-order nonchiral modal propagation around higher-order EPs in two \mathcal{T} -symmetric WGs. For instance, consider the four level Hamiltonian \mathcal{H} depends on three time-dependent parameters $\kappa_n(t)$ (for $n = 1, 2, 3$, analogous to $\gamma, \tau, \Delta n_{NL}$), where four modified eigenvalues are taken as $\beta_2^{ad}[\kappa_n(t)]$, $\beta_3^{ad}[\kappa_n(t)]$, $\beta_4^{ad}[\kappa_n(t)]$, $\beta_5^{ad}[\kappa_n(t)]$, and the corresponding eigenvectors are $\psi_2^{ad}[\kappa_n(t)]$, $\psi_3^{ad}[\kappa_n(t)]$, $\psi_4^{ad}[\kappa_n(t)]$, $\psi_5^{ad}[\kappa_n(t)]$, respectively. Here, under the adiabatic limit, the evaluation of the eigenfunction follows the time-dependent Schrödinger equation (TDSE). Here, both complementary variants show similar parametric dependency as they individually host higher-order conjugate EPs, which appear in the eigenvalues of the Hamiltonian. The time-dependent parameters $[\kappa_1(t), \kappa_2(t), \kappa_3(t)]$ control the nonadiabatic corrections in the TDSE associated with \mathcal{H} [57]. Such nonadiabatic correction factors around higher-order EPs during beam propagation can be written as

$$\mathcal{O}_{G \rightarrow H}^{NA} = \mathcal{U}_{G \rightarrow H} \exp \left\{ (+)i \int_0^T \Delta\beta_{G,H}^{ad}[\kappa_n(t)] dt \right\}, \quad (11a)$$

$$\mathcal{O}_{H \rightarrow G}^{NA} = \mathcal{U}_{H \rightarrow G} \exp \left\{ (-)i \int_0^T \Delta\beta_{G,H}^{ad}[\kappa_n(t)] dt \right\}, \quad (11b)$$

with the preexponent terms

$$\mathcal{U}_{G \rightarrow H} = \left\langle \psi_G^{ad}[\kappa_n(t)] \left| \sum_{m=1}^3 \dot{\kappa}_n \frac{\partial}{\partial \kappa_n} \right| \psi_H^{ad}[\kappa_n(t)] \right\rangle, \quad (12a)$$

$$\mathcal{U}_{H \rightarrow G} = \left\langle \psi_H^{ad}[\kappa_n(t)] \left| \sum_{m=1}^3 \dot{\kappa}_n \frac{\partial}{\partial \kappa_n} \right| \psi_G^{ad}[\kappa_n(t)] \right\rangle, \quad (12b)$$

$$\begin{aligned} \text{and } \Delta\beta_{G,H}^{ad}[\kappa_n(t)] &= \beta_G^{ad}[\kappa_n(t)] - \beta_H^{ad}[\kappa_n(t)] \\ &\equiv \text{Re}[\Delta\beta_{G,H}^{ad}\{\kappa_n(t)\}] \mp i\Delta\zeta_{G,H}^{ad}[\kappa_n(t)]. \end{aligned} \quad (12c)$$

In Eqs. (11) and (12), the suffixes $G \rightarrow H$ and $H \rightarrow G$ correspond to the conversion $\psi_G^{ad} \rightarrow \psi_H^{ad}$ and vice versa, respectively. T is the encirclement duration during evolution. Now, the preexponent terms $\mathcal{U}_{G \rightarrow H}$ and $\mathcal{U}_{H \rightarrow G}$, as given by Eqs. (12a) and (12b) contain the time derivative of $\kappa_n(t)$ (i.e., $\dot{\kappa}_n$). The exponential divergence in T of the exponent of Eq. (11) beats the $(1/T)$ suppression associated with $\mathcal{U}_{G \rightarrow H}$ and $\mathcal{U}_{H \rightarrow G}$. Thus, for slow parametric evolution around higher-order conjugate EPs, one of the interacting modes has a lower average path loss, and due to that, it evolves adiabatically, but other modes follow NAT.

In Eq. (12c), the minus or plus sign correspond to two different complimentary variants, i.e., WG_a and WG_c ,

respectively. If we substitute the term $\Delta\beta_{G,H}^{ad}$ in Eq. (11), the corresponding exponent terms for the two complimentary variants are the key elements dictating the dominate output during the propagation. So, for WG_a , if we consider a situation $\Delta\zeta_{G,H}^{ad} > 0$, then for $T \rightarrow \infty$, $\mathcal{O}_{G \rightarrow H}^{NA} \rightarrow \infty$ and $\mathcal{O}_{H \rightarrow G}^{NA} \rightarrow 0$, but for the WG_c case, at $T \rightarrow \infty$, $\mathcal{O}_{G \rightarrow H}^{NA} \rightarrow 0$, and $\mathcal{O}_{H \rightarrow G}^{NA} \rightarrow \infty$. Thus for very slow parametric evolution within the parametric limit, the mode conversion associates with nonadiabatic correction terms $\mathcal{O}_{H \rightarrow G}^{NA}$ (for WG_a) and $\mathcal{O}_{G \rightarrow H}^{NA}$ (for WG_c) follow the adiabatic expectation, but the conversion associated with other nonadiabatic correction terms $\mathcal{O}_{G \rightarrow H}^{NA}$ (for WG_a) and $\mathcal{O}_{H \rightarrow G}^{NA}$ (for WG_c) do not ensure these adiabatic expectations. In a similar way, we can set up the opposite condition for $\Delta\zeta_{G,H}^{ad} < 0$. So, in any of the specific dynamical parametric encirclement directions, only one state shows the adiabatic transition.

We can study possible adiabatic and nonadiabatic modal dynamics among the four interacting modes in our two complementary waveguides with the proper choice of G and H . Now, if we consider WG_a , the dynamical encirclement along Loop3 [as shown in Fig. 4(b.1)] in the presence of two different types of nonlinearity ($\sigma = +1$ or -1) in the optical medium of the WG, the refractive index profile and corresponding β values change depending on the types of nonlinearity, and accordingly, the sign of the relative gain factor ($\Delta\zeta_{G,H}^{ad}$) for different choice of G and H are modified. Here for considering the loops shown in Fig. 4(b), in addition to the relative gain factors between the coupled pairs, i.e., $\Delta\zeta_{2,3}^{ad}$ and $\Delta\zeta_{4,5}^{ad}$, there should be four other terms viz. $\Delta\zeta_{3,4}^{ad}$, $\Delta\zeta_{5,2}^{ad}$, $\Delta\zeta_{3,5}^{ad}$, and $\Delta\zeta_{4,2}^{ad}$ due to possible interactions among the four chosen coupled modes. Here, in the presence of FN ($\sigma = +1$) and considering both CW and CCW propagation, we observed that in WG_a , the terms $\Delta\zeta_{2,3}^{ad}$ and $\Delta\zeta_{3,5}^{ad}$ dominate over the other factors associated with nonadiabatic correction. So, we find the situations $\Delta\zeta_{2,3}^{ad} < 0$ (or > 0) and $\Delta\zeta_{3,5}^{ad} > 0$ (or < 0) for CW (or CCW) encirclement direction [as shown in Fig. 4(b.1)], which gives the conversion of $\{\psi_2, \psi_3, \psi_4, \psi_5\} \rightarrow \psi_4$, as shown in the Figs. 5(a) and 5(b). Thus, beyond the adiabatic expectations, $\Delta\zeta_{2,3}^{ad} > 0$ and $\Delta\zeta_{3,4}^{ad} < 0$, with an adiabatic transitions of $\psi_5 \rightarrow \psi_4$ for CW encirclement, however, $\Delta\zeta_{2,3}^{ad} > 0$ and $\Delta\zeta_{4,2}^{ad} > 0$, for CCW directions includes the adiabatic conversion of $\psi_3 \rightarrow \psi_4$. Now if we consider DFN ($\sigma = -1$) in the same loop, then we observe that $\Delta\zeta_{5,2}^{ad} < 0$ (or > 0) and $\Delta\zeta_{4,2}^{ad} < 0$ (or > 0) for CW (or CCW) encirclement directions, which gives the conversion of $\{\psi_2, \psi_3, \psi_4, \psi_5\} \rightarrow \psi_3$, as shown in Figs. 5(c) and 5(d). In this case, beyond the adiabatic expectations, $\psi_5(\rightarrow \psi_3)$ follows adiabatic conversion due to the two dominating factors $\Delta\zeta_{5,2}^{ad} < 0$ and $\Delta\zeta_{2,3}^{ad} < 0$ for the CW directions, but at the CCW condition, the terms $\Delta\zeta_{5,2}^{ad} > 0$ and $\Delta\zeta_{3,5}^{ad} > 0$ with an adiabatic transitions of $\psi_2 \rightarrow \psi_3$.

If we consider the WG_c variant and study the dynamical encirclement along Loop3 [Fig. 4(b.2)] in the presence of FN or DFN, we observe similar dynamics as shown in Fig. 6, which are similar to those in Fig. 5. To consider CW dynamical encirclement along the loop in the presence of FN ($\sigma = +1$), in the presence of other terms, we find the situations where the dominating factors are viz. $\Delta\zeta_{3,5}^{ad} < 0$, $\Delta\zeta_{3,4}^{ad} > 0$, and $\Delta\zeta_{5,2}^{ad} > 0$. Thus we get the situation where ψ_2

follows the adiabatic expectations. If we consider the CCW encirclement along the same loop, the dominating factors are $\Delta\zeta_{2,3}^{\text{ad}} < 0$, $\Delta\zeta_{5,2}^{\text{ad}} < 0$, and $\Delta\zeta_{4,2}^{\text{ad}} < 0$. In this case, ψ_5 follows the adiabatic transition. In both situations, we get the overall conversion of $(\psi_2, \psi_3, \psi_4, \psi_5) \rightarrow \psi_4$. On the other hand, for DFN ($\sigma = -1$) conditions, we observe that for CW encirclement, the dominating nonadiabatic factors are $\Delta\zeta_{5,2}^{\text{ad}} > 0$, $\Delta\zeta_{3,4}^{\text{ad}} < 0$, and $\Delta\zeta_{3,5}^{\text{ad}} < 0$. Here, ψ_2 follows the adiabatic transition. In addition, for CCW encirclement, the dominating factors are viz. $\Delta\zeta_{3,5}^{\text{ad}} < 0$, $\Delta\zeta_{2,3}^{\text{ad}} > 0$, and $\Delta\zeta_{4,5}^{\text{ad}} < 0$. Here, the ψ_4 follows adiabatic transition. These analytical predictions are supported by the beam propagation results illustrated in Figs. 5 and 6.

IV. CONCLUSION

In summary, we propose the concept of a nonlinearity-induced higher-order mode-collapsing phenomenon. This event occurs during a dynamic encirclement around higher-order conjugate exceptional points (EPs) in two multimodal, gain-loss-assisted planar waveguides. These waveguides are linked with \mathcal{T} -symmetric optical potentials grounded on complex refractive index profiles. Here, the multilayer gain-loss profiles vary in such a way that two complementary waveguide variants experience complex conjugate imaginary parts of the refractive index profiles, and both are correlated by \mathcal{T} symmetry. Instead of the reverse chiral response around a single pair of conjugate EP2, here we observed that, in

the absence of nonlinearity, two complementary waveguides exhibit nonchiral light dynamics around the conjugate EP3s even in the presence of other noninteracting modes. Now, with the onset of the nonlinearity, four interacting coupled modes collapse into a specific dominating higher-order mode (with higher conversion efficiencies) irrespective of the choice of the encirclement direction in both complementary WGs. Here, we establish that, based on the constraints of \mathcal{T} symmetry, the presence of the same amount of individual focusing and defocusing nonlinearities results in different dominating higher-order outputs for the same parametric encirclement process around higher-order conjugate EPs. The proposed scheme is enriched with the topology of higher-order conjugate EPs to investigate the inherent correlations between two \mathcal{T} -symmetric systems based on optical responses. We may also explore higher-order nonreciprocal light transmission through such complementary optical waveguides around higher-order conjugate EPs in the presence of nonlinearity. Applying this strategy to the proposed device will offer distinct opportunities. Particularly, it enables direction-dependent higher-order modal transport. Moreover, the feasibility of fabricating such a device would significantly impact chip-scale-integrated photonic systems.

ACKNOWLEDGMENT

S.D. acknowledges the support from the Ministry of Education (MoE), Government of India.

-
- [1] N. Moiseyev, *Non-Hermitian Quantum Mechanics* (Cambridge University Press, Cambridge, England, 2011).
- [2] T. Kato, *Perturbation Theory for Linear Operators* (Springer, Berlin, 1995).
- [3] E. J. Bergholtz, J. C. Budich, and F. K. Kunst, *Rev. Mod. Phys.* **93**, 015005 (2021).
- [4] W. D. Heiss and A. L. Sannino, *J. Phys. A: Math. Gen.* **23**, 1167 (1990).
- [5] W. D. Heiss, *Phys. Rev. E* **61**, 929 (2000).
- [6] G. Demange and E.-M. Graefe, *J. Phys. A: Math. Theor.* **45**, 025303 (2012).
- [7] W. D. Heiss and G. Wunner, *J. Phys. A: Math. Theor.* **49**, 495303 (2016).
- [8] Q. Wang, K. Ding, H. Liu, S. Zhu, and C. T. Chan, *Opt. Express* **28**, 1758 (2020).
- [9] C. Dembowski, H.-D. Gräf, H. L. Harney, A. Heine, W. D. Heiss, H. Rehfeld, and A. Richter, *Phys. Rev. Lett.* **86**, 787 (2001).
- [10] C. Hahn, Y. Choi, J. W. Yoon, S. H. Song, C. H. Oh, and P. Berini, *Nat. Commun.* **7**, 12201 (2016).
- [11] Y. Choi, S. Kang, S. Lim, W. Kim, J.-R. Kim, J.-H. Lee, and K. An, *Phys. Rev. Lett.* **104**, 153601 (2010).
- [12] X.-L. Zhang, S. Wang, B. Hou, and C. T. Chan, *Phys. Rev. X* **8**, 021066 (2018).
- [13] M. Müller and I. Rotter, *J. Phys. A: Math. Theor.* **41**, 244018 (2008).
- [14] W. D. Heiss, *J. Phys. A: Math. Theor.* **41**, 244010 (2008).
- [15] S. Bhattacharjee, A. Laha, and S. Ghosh, *Phys. Scr.* **94**, 105509 (2019).
- [16] H. Menke, M. Klett, H. Cartarius, J. Main, and G. Wunner, *Phys. Rev. A* **93**, 013401 (2016).
- [17] J.-W. Ryu, S.-Y. Lee, and S. W. Kim, *Phys. Rev. A* **85**, 042101 (2012).
- [18] Q. Zhong, M. Khajavikhan, D. N. Christodoulides, and R. El-Ganainy, *Nat. Commun.* **9**, 4808 (2018).
- [19] W. D. Heiss, *Eur. Phys. J. D* **7**, 1 (1999).
- [20] J. Doppler, A. A. Mailybaev, J. Böhm, U. Kuhl, A. Girschik, F. Libisch, T. J. Milburn, P. Rabl, N. Moiseyev, and S. Rotter, *Nature (London)* **537**, 76 (2016).
- [21] S. Dey, A. Laha, and S. Ghosh, *Opt. Commun.* **483**, 126644 (2021).
- [22] A. Roy, S. Dey, A. Laha, A. Biswas, and S. Ghosh, *Opt. Lett.* **47**, 2546 (2022).
- [23] Z.-X. Liu, C. You, B. Wang, H. Dong, H. Xiong, and Y. Wu, *Nanoscale* **12**, 2118 (2020).
- [24] D. A. Bykov and L. L. Doskolovich, *Phys. Rev. A* **97**, 013846 (2018).
- [25] S. Dey, A. Roy, and S. Ghosh, *Phys. Scr.* **97**, 085501 (2022).
- [26] H. Jing, Ş. Özdemir, H. Lü, and F. Nori, *Sci. Rep.* **7**, 3386 (2017).
- [27] J.-W. Zhang, J.-Q. Zhang, G.-Y. Ding, J.-C. Li, J.-T. Bu, B. Wang, L.-L. Yan, S.-L. Su, L. Chen, F. Nori, Ş. K. Özdemir, F. Zhou, H. Jing, and M. Feng, *Nat. Commun.* **13**, 6225 (2022).
- [28] A. Laha, D. Beniwal, S. Dey, A. Biswas, and S. Ghosh, *Phys. Rev. A* **101**, 063829 (2020).
- [29] R. Lefebvre, O. Atabek, M. Šindelka, and N. Moiseyev, *Phys. Rev. Lett.* **103**, 123003 (2009).

- [30] T.-X. Lu, H. Zhang, Q. Zhang, and H. Jing, *Phys. Rev. A* **103**, 063708 (2021).
- [31] C. Dembowski, B. Dietz, H.-D. Gräf, H. L. Harney, A. Heine, W. D. Heiss, and A. Richter, *Phys. Rev. E* **69**, 056216 (2004).
- [32] Ş. K. Özdemir, S. Rotter, F. Nori, and L. Yang, *Nat. Mater.* **18**, 783 (2019).
- [33] J. Wiersig, *Phys. Rev. A* **93**, 033809 (2016).
- [34] H. Hodaei, A. U. Hassan, S. Wittek, H. Garcia-Gracia, R. El-Ganainy, D. N. Christodoulides, and M. Khajavikhan, *Nature (London)* **548**, 187 (2017).
- [35] A. Suntharalingam, L. Fernández-Alcázar, R. Kononchuck, and T. Kottos, [arXiv:2303.10278](https://arxiv.org/abs/2303.10278).
- [36] J. Feilhauer, A. Schumer, J. Doppler, A. A. Mailybaev, J. Böhm, U. Kuhl, N. Moiseyev, and S. Rotter, *Phys. Rev. A* **102**, 040201(R) (2020).
- [37] Q. Liu, S. Li, B. Wang, S. Ke, C. Qin, K. Wang, W. Liu, D. Gao, P. Berini, and P. Lu, *Phys. Rev. Lett.* **124**, 153903 (2020).
- [38] H. K. Gandhi, A. Laha, S. Dey, and S. Ghosh, *Opt. Lett.* **45**, 1439 (2020).
- [39] B. Wang, Z.-X. Liu, C. Kong, H. Xiong, and Y. Wu, *Opt. Express* **27**, 8069 (2019).
- [40] R. Huang, Ş. Özdemir, J.-Q. Liao, F. Minganti, L.-M. Kuang, F. Nori, and H. Jing, *Laser Photon. Rev.* **16**, 2270034 (2022).
- [41] Y. Zuo, R. Huang, L.-M. Kuang, X.-W. Xu, and H. Jing, *Phys. Rev. A* **106**, 043715 (2022).
- [42] H. Hodaei, A. U. Hassan, W. E. Hayenga, M. A. Miri, D. N. Christodoulides, and M. Khajavikhan, *Opt. Lett.* **41**, 3049 (2016).
- [43] C. Wang, W. R. Sweeney, A. D. Stone, and L. Yang, *Science* **373**, 1261 (2021).
- [44] R. Thomas, H. Li, F. M. Ellis, and T. Kottos, *Phys. Rev. A* **94**, 043829 (2016).
- [45] Y. Choi, C. Hahn, J. W. Yoon, S. H. Song, and P. Berini, *Nat. Commun.* **8**, 14154 (2017).
- [46] A. Laha, S. Dey, H. K. Gandhi, A. Biswas, and S. Ghosh, *ACS Photon.* **7**, 967 (2020).
- [47] H. Lü, C. Wang, L. Yang, and H. Jing, *Phys. Rev. Appl.* **10**, 014006 (2018).
- [48] X.-H. Lu, L.-G. Si, X.-Y. Wang, and Y. Wu, *Opt. Express* **29**, 4875 (2021).
- [49] H. Jing, S. K. Özdemir, X.-Y. Lü, J. Zhang, L. Yang, and F. Nori, *Phys. Rev. Lett.* **113**, 053604 (2014).
- [50] M. Benzaouia, A. Stone, and S. G. Johnson, *APL Photon.* **7**, 121303 (2022).
- [51] A. U. Hassan, H. Hodaei, M.-A. Miri, M. Khajavikhan, and D. N. Christodoulides, *Phys. Rev. A* **92**, 063807 (2015).
- [52] Y. Zhiyenbayev, Y. Kominis, C. Valagiannopoulos, V. Kovanis, and A. Bountis, *Phys. Rev. A* **100**, 043834 (2019).
- [53] D. Kaltsas, I. Komis, and K. G. Makris, *Opt. Lett.* **47**, 4447 (2022).
- [54] B. Midya, H. Zhao, and L. Feng, *Nat. Commun.* **9**, 2674 (2018).
- [55] M. V. Berry, *Czech. J. Phys.* **54**, 1039 (2004).
- [56] H. Xu, D. Mason, L. Jiang, and J. Harris, *Nature (London)* **537**, 80 (2016).
- [57] I. Gilary, A. A. Mailybaev, and N. Moiseyev, *Phys. Rev. A* **88**, 010102(R) (2013).
- [58] X.-L. Zhang and C. T. Chan, *Commun. Phys.* **2**, 63 (2019).
- [59] A. Laha, S. Dey, and S. Ghosh, *Phys. Rev. A* **105**, 022203 (2022).
- [60] G. P. Agrawal, *Nonlinear Fiber Optics*, 5th ed. (Academic Press, New York, 2012).